Thermal Nanofluid Property Model With Application to Nanofluid Flow in a Parallel Disk System—Part II: Nanofluid Flow Between Parallel Disks

Yu Feng

Clement Kleinstreuer[1]
e-mail: ck@eos.ncsu.edu

Department of Mechanical
and Aerospace Engineering,
North Carolina State University,
Raleigh, NC 27695-7910

This is the second part of a two-part paper which proposes a new theory explaining the experimentally observed enhancement of the thermal conductivity, k_{nf}, of nanofluids (Part I) and discusses simulation results of nanofluid flow in an axisymmetric jet-impingement cooling system using different k_{nf}-models (Part II). Specifically, Part II provides numerical simulations of convective nanofluid heat transfer in terms of velocity profiles, friction factor, temperature distributions, and Nusselt numbers, employing the new k_{nf}-model. Flow structures and the effects of nanoparticle addition on heat transfer and entropy generation are discussed as well. Analytical expressions for velocity profiles and friction factors, assuming quasi-fully-developed flow between parallel disks, have been derived and validated for nanofluids as well. Based on the numerical simulation results for both alumina-water nanofluids and pure water, it can be concluded that nanofluids show better heat transfer performance than convectional coolants with no great penalty in pumping power. Furthermore, the system's entropy generation rate is lower for nanofluids than for pure water. [DOI: 10.1115/1.4005633]

Keywords: nanofluid flow, augmented heat transfer, parallel disk system

1 Introduction

In addition to the possible thermal conductivity enhancement, dilute nanoparticle suspensions exhibit other advantages over the use of micron particles, e.g., insignificant erosion to an apparatus, more stable dispersions, small aggregation effects, and no filter-clogging. Thus, applications of nanofluid flow with potentially elevated convective heat transfer performance for microscale cooling systems are of great importance [1].

As a test case, a jet-impingement, radial flow cooling system consisting of a supply tube and two parallel coaxial disks [2] was investigated (see Fig. 1(*a*)). It features many technical applications related to lubrication, viscometers, heat exchangers and biomedical devices. Related publications include Winter [3], focusing on molten polymers flow, who provided an approximate solution for flow between two parallel disks with a centered inlet and experimentally measured fluid flow parameters. Szeri et al. [4] reviewed experimental and theoretical papers concerning different disk flows. They concluded that the quasi-fully-developed velocity profile is parabolic, and that at midradius, the flow field is quite independent of the radial boundary conditions, a fact which has been confirmed in the validation part of this paper. Mochizuki and Yang [5] experimentally investigated the heat transfer performance of parallel disks with a heat flux at the upper disk at constant power supply, presenting the Nusselt number in the r-direction for different Reynolds numbers. More recently, Nakabayashi et al. [6] investigated flow separation and reattachment, subject to different geometric parameters and Reynolds numbers by dye filament techniques. Achintya [7] provided an analytic solution of thermal radial flow between two parallel disks. While all contributions so far were for pure fluids, Roy and his group published a series of experimental and numerical heat transfer papers, using nanofluids [2,8–11]. However, their nanofluid simulation results relied on the Maxwell theory for the thermal conductivity of the mixture. Furthermore, the present paper provides new physical insight via the use of the new, experimentally validated k_{nf}-model (see Part I) and visualization of the flow structures as well as temperature fields of the cooling system based on a two-way coupled solution procedure. Specifically, the convective heat transfer enhancement capabilities are evaluated (i.e., Nusselt number, friction factor, and pressure drop) for nanofluids of different volume fractions (φ), inlet Reynolds numbers (Re), and spacing (δ) between the two parallel disks. Other competitive thermal conductivity models are also compared to experimental data sets. Thermal device-performance improvements, based on minimization of entropy generation, are discussed as well.

2 Theory

The dilute suspensions of nanoparticles in water of the present radial cooling system (see Fig. 1) are assumed to be Newtonian mixtures in steady 3D laminar nonisothermal flow.

2.1 Governing Equations

2.1.1 Continuity Equation

$$\nabla \cdot \vec{v} = 0 \tag{1}$$

2.1.2 Momentum Equation

$$\vec{v} \cdot \nabla \vec{v} = \frac{1}{\rho_{nf}} \nabla p + \frac{\mu_{nf}}{\rho_{nf}} \nabla^2 \vec{v} + \vec{g} \tag{2}$$

[1]Corresponding author.

Contributed by the Heat Transfer Division of ASME for publication in the JOURNAL OF HEAT TRANSFER. Manuscript received April 5, 2010; final manuscript received November 5, 2010; published online April 11, 2012. Assoc. Editor: Ping Cheng.

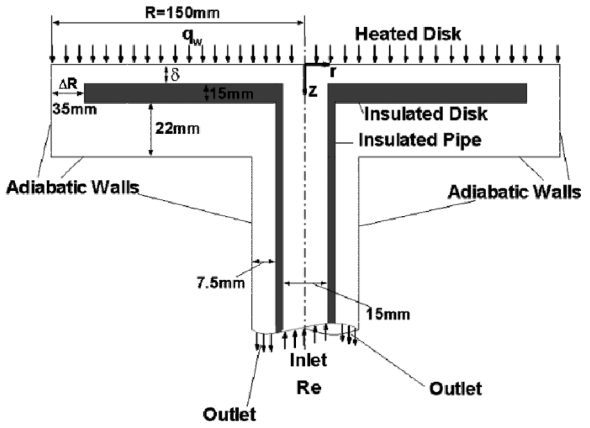

(a)

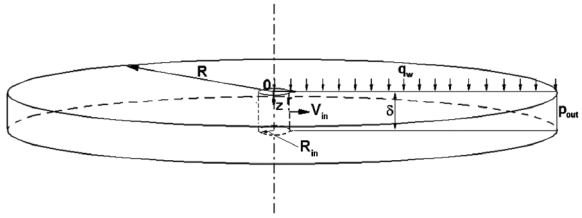

(b)

Fig. 1 (*a*) Sketch of the radial flow cooling system and (*b*) simplified model of the cooling system

2.1.3 Energy Equation

$$\vec{v}\cdot\nabla T=\frac{\nabla\cdot(k_{nf}\nabla T)}{(\rho c_p)_{nf}}+\frac{\Phi}{(\rho c_p)_{nf}} \tag{3}$$

where Φ is the shear stress induced heat dissipation in cylindrical coordinates, i.e.,

$$\Phi=\mu_{nf}\left\{\left(\frac{\partial v_\theta}{\partial z}+\frac{1}{r}\frac{\partial v_z}{\partial\theta}\right)^2+\left(\frac{\partial v_z}{\partial r}+\frac{\partial v_r}{\partial z}\right)^2+\left(\frac{1}{r}\frac{\partial v_r}{\partial\theta}+r\frac{\partial}{\partial r}\left(\frac{\partial v_\theta}{\partial r}\right)\right)^2+2\left(\left(\frac{\partial v_r}{\partial r}\right)^2+\left(\frac{1}{r}\left(\frac{\partial v_\theta}{\partial\theta}+v_r\right)\right)^2+\left(\frac{\partial v_z}{\partial z}\right)^2\right)\right\} \tag{4}$$

2.1.4 Boundary Conditions. As indicated in Fig. 1, we assume uniform inlet velocity and pressure outlet, constant wall heat flux q_w, no-slip condition at the heated upper disk ($r\in[0,R], z=0$) as well as adiabatic and no-slip conditions at all other walls.

2.1.5 Nanofluid Properties. The basic nanofluid properties are a function of nanoparticle volume fraction φ and mixture temperature T. Such nanofluids are assumed to be dilute suspensions, i.e., the homogeneous, noninteracting nanoparticles are well dispersed. Specifically, for dilute Al_2O_3-water nanofluids [12]

$$\mu_{nf}=\mu_{bf}\frac{1}{(1-\varphi)^{2.5}} \tag{5a}$$

$$\rho_{nf}=\varphi\rho_p+(1-\varphi)\rho_{bf} \tag{5b}$$

$$(\rho c_p)_{nf}=\varphi(\rho c_p)_p+(1-\varphi)(\rho c_p)_{bf} \tag{5c}$$

For the effective thermal conductivity of the nanofluid, the newly developed Feng-Kleinstreuer (F-K) model (see Part I) was applied. In summary, it was postulated that the thermal conductivity of nanofluids consists of a static part (k_{static}) after Maxwell [13] and a micromixing part (k_{mm}), i.e., enhancement due to Brownian motion of nanoparticles. Thus, k_{nf} of the F-K model is expressed as

$$k_{nf}=k_{static}+k_{mm} \tag{6}$$

The static part is given by Maxwell's model as

$$k_{static}=\left(1+\frac{3\left(\frac{k_p}{k_{bf}}-1\right)\varphi}{\left(\frac{k_p}{k_{bf}}+2\right)-\left(\frac{k_p}{k_{bf}}-1\right)\varphi}\right)k_{bf} \tag{7}$$

while the micromixing part is given by (see Part I)

$$k_{mm}=49,500\cdot\frac{\kappa_B\tau_p}{2m_p}\cdot C_c\cdot(\rho c_p)_{nf}\cdot\varphi^2\cdot(T\ln T-T)\cdot\frac{\exp(-\zeta\omega_n\tau_p)\sinh\left(\sqrt{\frac{(3\pi\mu_{bf}d_p)^2}{4m_p^2}-\frac{K_{P-P}}{m_p}}\frac{m_p}{3\pi\mu_{bf}d_p}\right)}{\tau_p\sqrt{\frac{(3\pi\mu_{bf}d_p)^2}{4m_p^2}-\frac{K_{P-P}}{m_p}}} \tag{8}$$

Here, ρ is the density, c_p is the specific heat capacity, φ is the nanoparticle volume fraction, while the subscripts nf, bf, and p indicate nanofluid, base fluid and particle, respectively. C_c is equal to 38 for metal-oxide nanofluids which can be derived theoretically (which also holds for the number 49,500), instead of being obtained via a curve-fitting technique [14]. The damping coefficient ζ, natural frequency ω_n, and characteristic time interval τ_p can be expressed as

$$\zeta=\frac{3\pi d_p\mu_{bf}}{2m_p\omega_n} \tag{9}$$

$$\omega_n=\sqrt{\frac{K_{P-P}}{m_p}} \tag{10}$$

$$\tau_p=\frac{m_p}{3\pi\mu_{bf}d_p} \tag{11}$$

Specifically, for metal-oxide nanofluids, the magnitude of particle–particle interaction intensity K_{P-P} (or stiffness) is determined as

$$K_{P-P}=\rho_p\cdot\sqrt{d_p}\cdot\left(\frac{32.1724\cdot 273K}{T}-19.4849\right) \tag{12}$$

In light of experimental evidence, the F-K model is suitable for several types of metal-oxide nanoparticles ($20<d_p<50$ nm) in water with volume fractions up to 5%, and mixture temperatures below 350 K. The properties of the base fluid, i.e., water, vary with temperature as follows [12]:

$$\rho_{water}=1000\cdot\left(1-\frac{(T+15.7914)}{508929.2\cdot(T-205.0204)}\cdot(T-277.1363)^2\right) \tag{13a}$$

$$c_{p,water} = 9616.8734 - 48.7365 \cdot T + 0.1445 \cdot T^2 - 0.0001414 \cdot T^3 \tag{13b}$$

$$\mu_{water} = 0.02165 - 0.0001208 \cdot T + 1.7184e - 7 \cdot T^2 \tag{13c}$$

$$k_{water} = -1.1245 + 0.009734 \cdot T - 0.00001315 \cdot T^2 \tag{13d}$$

Different types of nanofluids were employed in the application of nanofluid flow between parallel disks.

2.2 Reduced Modeling Equations. For radial nanofluid flow between two parallel disks (see Fig. 1(*b*), $r \in [R_{in}, R], z \in [0, \delta]$), the governing Eqs. (1)–(3) can be reduced to

$$\frac{v_r}{r} + \frac{\partial v_r}{\partial r} = 0 \tag{14}$$

$$\frac{\partial^2 v_r}{\partial z^2} = \frac{1}{\mu_{nf}}\frac{\partial p}{\partial r} + \frac{1}{\upsilon_{nf}} v_r \frac{\partial v_r}{\partial r} \tag{15a}$$

With $\frac{R-R_{in}}{R_{in}}$ being very small, $\frac{\partial v_r}{\partial r} \ll \frac{\partial p}{\partial r}$ and hence, Eq. (15*a*) can be further reduced to

$$\frac{\partial^2 v_r}{\partial z^2} = \frac{1}{\mu_{nf}}\frac{\partial p}{\partial r} \tag{15b}$$

and in the z-direction

$$\frac{1}{\rho_{nf}}\frac{\partial p}{\partial z} = 0 \tag{15c}$$

$$(\rho c_p)_{nf} vr \frac{\partial T}{\partial r} = \left(\frac{1}{r}\frac{\partial}{\partial r}\left(K_{nf}\left(r\frac{\partial T}{\partial r}\right)\right) + \frac{\partial^2 T}{\partial z^2}\right) + \Phi \tag{16}$$

where Φ can be reduced to

$$\Phi = \mu_{nf}\left(\left(\frac{\partial v_r}{\partial z}\right)^2 + 2\left(\frac{\partial v_r}{\partial r}\right)^2 + 2\left(\frac{v_r}{r}\right)^2\right) \tag{17}$$

The boundary conditions are

$$v_r(r = R_{in}) = V_{in} \tag{18a}$$

$$v_r(z = 0) = 0 \tag{18b}$$

$$v_r(z = \delta) = 0 \tag{18c}$$

$$p(r = R) = p_2 \tag{18d}$$

$$k_{nf}\left.\frac{\partial T}{\partial z}\right|_{z=0} = qw \tag{18e}$$

$$\left.\frac{\partial T}{\partial z}\right|_{z=\delta} = 0 \tag{18f}$$

2.3 Velocity Profiles and Temperature Distributions. According to Figs. 1(*a*) and 1(*b*), the inlet flow rate can be written as

$$Q_{in} = 2\pi R_{in} \cdot \delta \cdot V_{in} \tag{19}$$

From Eq. (13), we obtain that p is only a function of r, so that after integration of Eq. (15*b*)

$$v_r = -\frac{1}{2\mu_{nf}}\frac{dp}{dr}(\delta - z)z \tag{20}$$

Based on mass conservation

$$Q(r) = \int_0^\delta 2\pi r \cdot u dz = Q_{in} = 2\pi R_{in} \cdot \delta \cdot V_{in} \tag{21}$$

so that

$$p(r) = \frac{12\mu_{nf} R_{in} V_{in}}{\delta^2} \cdot \ln\left(\frac{R}{r}\right) + p_2 \tag{22}$$

and Eq. (20) can now be rewritten as

$$v_r = \frac{6R_{in}V_{in}}{\delta^2} \cdot \frac{1}{r} \cdot (\delta - z) \cdot z \tag{23a}$$

or in nondimensionalized form

$$\tilde{v}_r = 6\left(\frac{R_{in}}{R}\right) \cdot \frac{1}{\tilde{r}} \cdot (1 - \tilde{z}) \cdot \tilde{z} \tag{23b}$$

where

$$\tilde{v}_r = \frac{v_r}{V_{in}} \tag{24a}$$

$$\tilde{r} = \frac{r}{R} \tag{24b}$$

$$\tilde{z} = \frac{z}{\delta} \tag{24c}$$

With Eqs. (23*b*) and (18), we obtain

$$\Phi = \mu_{nf}\frac{6R_{in}V_{in}}{\delta^2}\left(\left(\frac{\delta - 2z}{r}\right)^2 + \frac{4(\delta - z)^2 z^2}{r^4}\right) \tag{25}$$

Hence, Eq. (17) can be expressed as

$$(\rho c_p)_{nf} v_r \frac{\partial T}{\partial r} = k_{nf}\left(\frac{1}{r}\frac{\partial}{\partial r}\left(r\frac{\partial T}{\partial r}\right) + \frac{\partial^2 T}{\partial z^2}\right) + \mu_{nf}\frac{6R_{in}V_{in}}{\delta^2}\left(\left(\frac{\delta - 2z}{r}\right)^2 + \frac{4(\delta - z)^2 z^2}{r^4}\right) \tag{26}$$

Based on the geometric dimension shown in Fig. 1(*a*) and a relative order-of-magnitude analysis

$$\frac{1}{r}\frac{\partial}{\partial r}\left(r\frac{\partial T}{\partial r}\right) \ll \frac{\partial^2 T}{\partial z^2} \tag{27a}$$

$$\Phi \ll k_{nf}\frac{\partial^2 T}{\partial z^2} \tag{27b}$$

As a result, Eq. (17) can be further reduced to

$$(\rho c_p)_{nf} v_r \frac{\partial T}{\partial r} = \frac{\partial}{\partial z}\left(k_{nf}\frac{\partial T}{\partial z}\right) \tag{28}$$

with boundary conditions (18*e*) and (18*f*) as well as

$$T(r = 0) = T_{in} \tag{29}$$

Equation (28) was solved, using MAPLE 12.0, in terms of an infinite series of hypergeometric functions.

2.4 Friction Factor and Pressure Drop. The Darcy-Moody friction factor f_D is defined as [15]

$$f_D = \frac{4\tau_w}{\frac{1}{2}\rho\bar{v}^2} \tag{30}$$

where τ_w is the shear stress at the wall, ρ is the fluid density, and $\overline{v}$ is the average velocity of the flow at different r-stations.

Specifically, for nanofluid flow between simplified model for parallel disks (see Fig. 1(*b*)), the velocity profile is given by Eq. (23*a*). Hence, the wall shear stress can be expressed as

$$\tau_w = \mu_{nf}\left.\frac{\partial v_z}{\partial z}\right|_{z=\delta} = \frac{6\mu_{nf}R_{in}V_{in}}{\delta}\cdot\frac{1}{r} \tag{31}$$

The average velocity $\overline{v_z}$ in terms of V_{in} reads

$$\overline{v_z} = \frac{R_{in}}{r}V_{in} \tag{32}$$

Hence, the local friction factor reads

$$f_D = \frac{96\mu_{nf}r}{\rho_{nf}R_{in}V_{in}\delta} = \frac{96}{Re_{nf}^{in}}\cdot\frac{2\delta}{R_{in}}\cdot\frac{r}{R_{in}} \qquad r\in[R_{in},R] \tag{33}$$

where $Re_{nf}^{in} = \rho_{nf}V_{in}R_{in}/\mu_{nf}$ is the inlet Reynolds number of the nanofluid and R_{in} is the inlet radius. The average friction factor $\overline{f_D}$ can be obtained after integration

$$\overline{f_D} = \frac{\int_{R_{in}}^{R}\int_0^{2\pi} f_D\cdot r\,d\theta\cdot dr}{2\pi\left(R^2-R_{in}^2\right)\delta} \tag{34}$$

and being a function of R, R_{in}, and Re_{nf}^{in}.

For the cooling system (see Fig. 1(*a*)), the friction factor f_D depends on the following parameters:

$$f_D = \text{fcn}\cdot\left\{\mu_{nf},\rho_{nf},k_{nf},d_p,\varphi,T_{in},q_w\right\} \tag{35}$$

which can be expressed in terms of four dimensionless groups

$$f_D = \text{fcn}\cdot\left\{Re_{nf}^{in},\frac{d_p}{\delta},\varphi,Nu_{in}=\frac{qw\cdot(2\delta)}{T_{in}\cdot k_{nf}}\right\} \tag{36a}$$

Considering that Eqs. (5*a*) and (5*b*) exhibit no dependence on particle diameter d_p, for constant spacing δ, Eq. (36*a*) can be simplified to

$$f_D = \text{fcn}\cdot\left\{Re_{nf}^{in},\varphi,Nu_{in}=\frac{q_w\cdot(2\delta)}{T_{in}\cdot k_{nf}}\right\} \tag{36b}$$

The equation of motion in the r-direction for the representative element volume in cylindrical coordinates [14] can be written as

$$p\cdot r\cdot d\theta\cdot\delta-(p+dp)\cdot r\cdot d\theta\cdot\delta-2\cdot\tau_w\cdot r\cdot d\theta\cdot dr=0 \tag{37}$$

which results in

$$-\frac{dp}{dr} = 2\tau_w \tag{38}$$

subject to

$$p(r=R)=0 \tag{39}$$

so that

$$p(r) = \frac{12\mu_{nf}R_{in}V_{in}}{\delta^2}\cdot\ln\left(\frac{R}{r}\right) \tag{40a}$$

$$p = Re_{nf}^{in}\cdot\frac{6\mu_{nf}^2R_{in}^2}{\rho_{nf}\delta^4}\cdot\ln\left(\frac{R}{r}\right) \tag{40b}$$

For the pressure drop Δp between inlet ($r=R_{in}$) and outlet ($r=R$) is

$$\Delta p = \frac{12\mu_{nf}R_{in}V_{in}}{\delta^2}\cdot\ln\left(\frac{R}{R_{in}}\right) \tag{41a}$$

$$\Delta p = Re_{nf}^{in}\cdot\frac{6\mu_{nf}^2R_{in}^2}{\rho_{nf}\delta^4}\cdot\ln\left(\frac{R}{R_{in}}\right) \tag{41b}$$

2.5 Entropy Generation. The entropy generation rate per unit volume can be expressed as [16]

$$\dot{S}_{gen}''' = \frac{k}{T^2}(\nabla T)^2+\frac{\Phi}{T} \tag{42}$$

Thus, $\dot{S}_{gen}'''$ is caused by heat transfer and frictional effects, i.e.,

$$\dot{S}_{gen}^{'''(H)} = \frac{k}{T^2}(\nabla T)^2 \tag{43a}$$

and

$$\dot{S}_{gen}^{'''(F)} = \frac{\Phi}{T} \tag{43b}$$

For the quasi-fully-developed flow region, substituting Eq. (23) into Eq. (43*b*) yields

$$\dot{S}_{gen}^{'''(F)} = \frac{\mu_{nf}}{T}\cdot\left[\frac{6R_{in}V_{in}}{\delta^2}\frac{1}{r}(\delta-2z)\right]^2 \tag{44}$$

Now, in order to estimate the impact of $\dot{S}_{gen}^{'''(F)}$ versus $\dot{S}_{gen}^{'''(H)}$, entropy generation in Al_2O_3-water (4%; $d_p=47$ nm) with inlet mass flow rate 0.019 kg/s and heat flux $q_w=2438$ W/m^2 was numerically investigated. Specifically, for quasi-fully-developed flow we can form the ratio

$$\frac{\dot{S}_{gen}^{'''(H)}}{\dot{S}_{gen}^{'''(F)}} = \frac{\frac{k}{T}(\nabla T)^2}{\mu_{nf}\left[\frac{6R_{in}V_{in}}{\delta^2}\frac{1}{r}(\delta-2z)\right]^2} \tag{45}$$

After substituting all parameter values and integrating over the entire flow region (see Fig. 1(*b*)), Eq. (45) is of the order of 4×10^3. Hence, for the cooling system under investigation the frictional entropy generation rate $\dot{S}_{gen}^{(F)}$ can be neglected when compared to the heat transfer entropy generation rate $\dot{S}_{gen}^{(H)}$.

3 Numerical Method

As shown in Fig. 2, two symmetric surfaces were established to reduce computer simulation cost. The numerical solutions were executed with a user-enhanced finite volume method, i.e., ANSYS-CFX 11.0 and 12.0 from Ansys, Inc. (Canonsburg, PA). The computations were performed on an IBM Linux Cluster at North Carolina State University's High Performance Computing Center (Raleigh, NC) and on a local dual Xeon Intel 3.0G Dell desktop (C M-P Laboratory, MAE Department, NC State University). The unstructured mesh for the $\delta=3$ mm model contained 765,767 hexahedra elements with 816,822 nodes. In light of the large velocity and temperature gradients, which exist at the corners and near the boundaries, the mesh was refined locally by a factor of 1.05 (see Fig. 2). For the $\delta=2$ mm model, the same unstructured mesh-generation method was employed. The criterion of convergence was 1×10^{-5} for the maximum residual which guaranteed an average residual of less than 1×10^{-6} both for momentum and heat transfer. Mesh independence was examined and verified by increasing the nodal number by 100% which produced a maximum result change of just 2.53%. A typical numerical simulation case took 28–38 h. Additional model validation was achieved by comparing numerical results of velocity and temperature fields

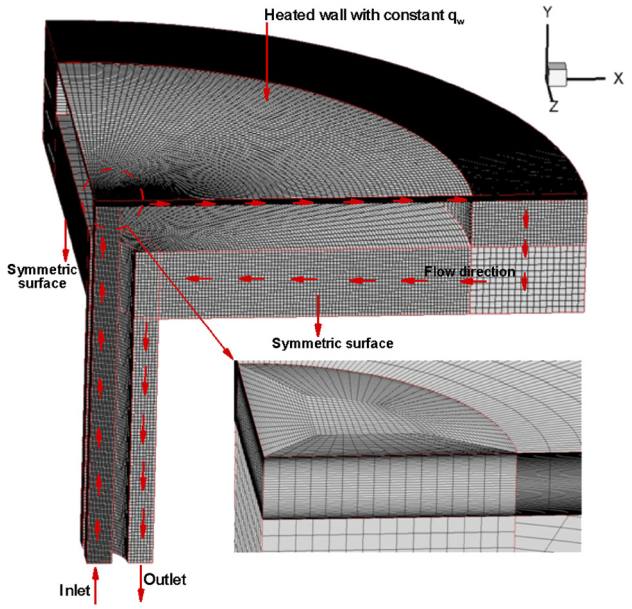

Fig. 2 Mesh details for the cooling system

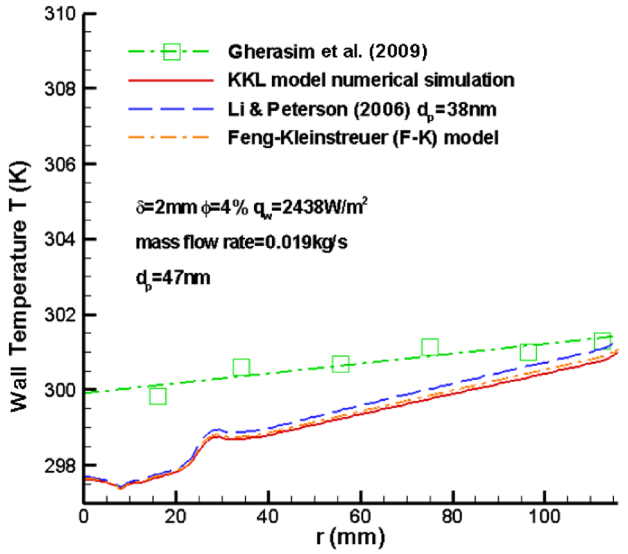

Fig. 4 Numerical simulation results for wall temperature distribution along r-direction by different thermal conductivity models and correlations

with our analytical solution as well as existing numerical and experimental data sets.

4 Results and Discussion

4.1 Model Validations

4.1.1 Comparison of Analytical Velocity Profiles and Numerical Results. Clearly, the geometry of the actual cooling system of Fig. 1(*a*) is more complicated than the simplified version (see Fig. 1(*b*)). Hence, it is of interest to compare Eq. (23) with the radial development of the actual velocity profile in light of the fully-developed flow assumption. As a test case, the $\delta = 3$ mm model with $\varphi = 4\%$ Al_2O_3-water mixture of $Re = 500$ (defined as $Re = (V_{in} \cdot 2\delta)/\nu_{nf}$) and heat flux $q_w = 3900$ W/m^2 was selected (see Fig. 3). The maximum error between velocity profiles at the same z station was 1.72%, due to the simplification of the nonlinear term $\frac{1}{\nu_{nf}} v_r \frac{\partial v_r}{\partial r}$ which was based on the assumption that $\frac{R-R_{in}}{R_{in}}$ is very small. For the $\delta = 2$ mm model the error dropped below 1%. It was also discovered that at $r/R = 0.7541$, in contrast to the Poiseuille-type solution, the numerical velocity profile is not symmetric to $z/\delta = 0.5$. Such a phenomenon is reasonable because the position at $r/R = 0.7541$ is very near the end of the lower disk, i.e., when $r/R = 0.7666$, which implies that the asymmetric velocity profile is due to the influence of the disk's end effect which draws the flow down toward the lower disk side. Nevertheless, in the quasi-developed region Eq. (23) is an acceptable approximation for the present parallel disk problem.

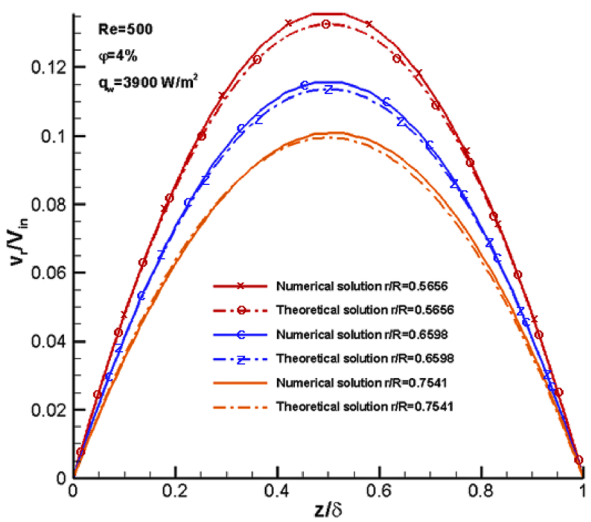

Fig. 3 Velocity profiles comparison between numerical solution and simplified theoretical solution for $\delta = 3$ mm

4.1.2 Comparison of Wall Temperature Distributions and Nusselt Number Results. Of interest is how the effective thermal conductivity model incorporated by Gherasim et al. compares to the new F-K model (see Part I) and another comparable theory (i.e., the KKL-model of Kleinstreuer and Li [12]) as well as measured data. Figure 4 shows the radial wall temperatures for a 2% Al_2O_3-water nanofluid with heat flux $q_w = 2438$ W/m^2 and $\dot{m} = 0.019$ kg/s. Clearly, although the trends of all distributions are similar there is a large difference in the region $0 < r < 100$ mm when compared to the results of Gherasim et al. [2]. It is worth mentioning that the nonlinearities appearing in the wall temperature curves of the computational results (see Fig. 4) are due to vortices appearing in the velocity field, which leads to slow flow circulation and thereby enhancing the local temperature. Interestingly, beyond the lower disk inlet zone, the radial Nusselt number results compare well with the measurements of Gherasim et al. [2], as given in Fig. 5. So, the discrepancy appearing in Fig. 4 resides in the calculation of the Nusselt number, where the subtraction of (not accurately measured) wall temperature and bulk temperature largely cancels out any measurable difference (see Fig. 5). Actually, a (local) disagreement between our numerical simulation result and the experimental data exist near the inlet between the parallel disks. The flow field is complicated near such a region (please refer to Fig. 7) and certain measurement techniques may fail to produce accurate observations. Thus, the local disagreement should be due to experimental errors.

4.2 Fluid Flow Structures. Figure 6 shows the velocity profile development between parallel disks in radial direction, with evidence of the back flow regions, i.e., $v_r < 0$. Similar results have been reported by Roy et al. [8] and Maiga et al. [10] numerically as well as experimentally by McGinn [17] and Nakabayashi [6]. This is physically reasonable; because, with higher Reynolds numbers the flow energy increases which causes, after "collision" with the disk, an undulating stream which forms the vortices (see

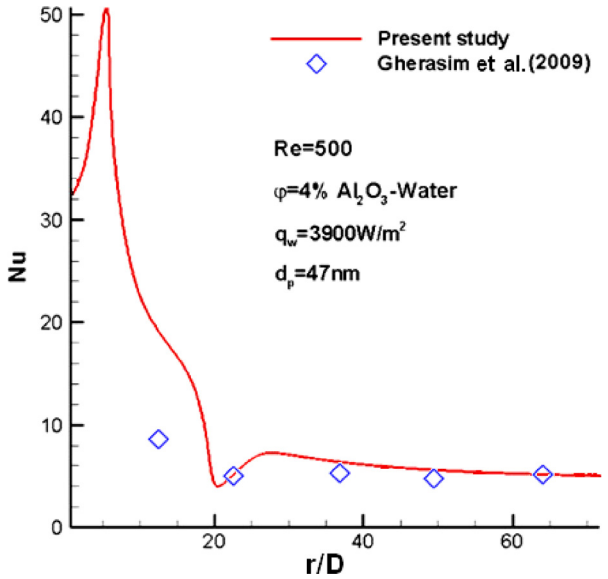

Fig. 5 Nusselt number comparison between present numerical simulation and experimental data

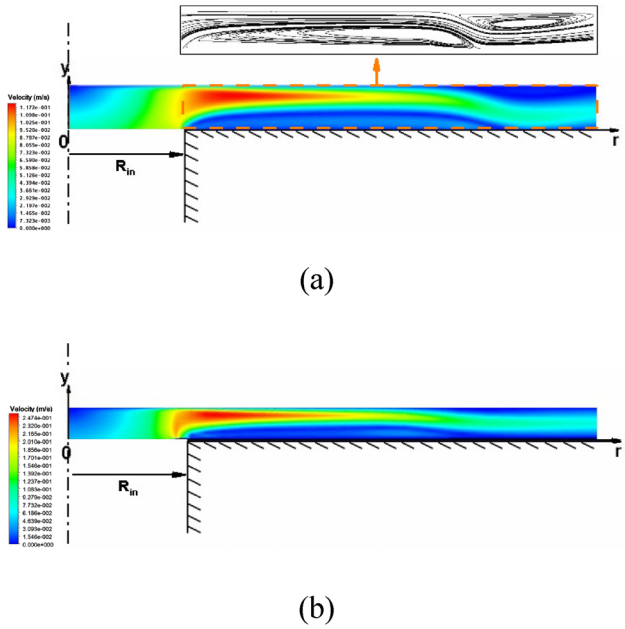

Fig. 7 Flow structure for flow between parallel disks (*a*) $\delta = 3$ mm and (*b*) $\delta = 2$ mm

Fig. 7(*a*)). Indeed, when comparing the velocity contours for different inlet Reynolds numbers, i.e., Re = 50, 200, and 500, it reveals that lower inlet Reynolds number do not cause such vortical flow structures [14].

The flow fields in the entrance region between parallel disks with different spacing (i.e., $\delta = 3$ mm and $\delta = 2$ mm) and same inlet Reynolds number Re = 500 were compared in Figs. 7(a) and 7(b). It can be easily observed that for $\delta = 2$ mm case (see Fig. 7(b)), the second vortex is small compared to the $\delta = 3$ mm case. Actually, the second vortex is very strongly influenced by wall temperature changes along the r-direction (see Sec. 4.4). Hence, for small δ-values, the second vortex can be well controlled and thereby the wall temperature influence.

4.3 Pressure Drop and Friction Factor

4.3.1 Pressure Drop. For a 4% $d_p = 47$ nm Al_2O_3-water nanofluid case, considering different inlet Reynolds numbers, examination of the radial pressure distributions indicated that dilute nanoparticle suspensions cause little enhancement in Δp when compared to pure water, implying that there will be no significant penalty on pumping power for cooling applications. Additionally, no dependence between pressure p and particle diameter $d_p < 60$ nm was observed [14].

4.3.2 Friction Factor. Considering the friction factor for the 4% $d_p = 38.4$ nm Al_2O_3-water nanofluid case, the impact of different inlet Reynolds numbers, inlet temperatures, volume fractions, and particle diameters were investigated and the numerical results (see model in Fig. 1(*a*)) were compared to the analytic solution (see model in Fig 1(*b*)). For a fixed spacing δ and fixed wall heat flux q_w, the relationship between f_D and T_{in} reflects the correlation between f_D and Nu. The comparisons between numerical simulations and theoretical predictions (see Eq. (33)) for inlet temperatures $T_{in} = 297$ K and $T_{in} = 308$ K are shown in Fig. 8. In the inlet region $0 < r < 0.06$ m (see Fig. 1(*a*)), the numerical simulations

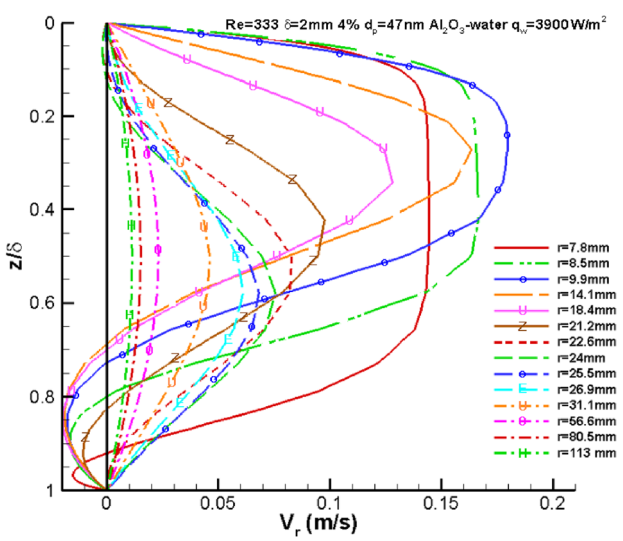

Fig. 6 Velocity profile development for $\delta = 2$ mm 4% Al_2O_3-water nanofluid with Re = 333.33

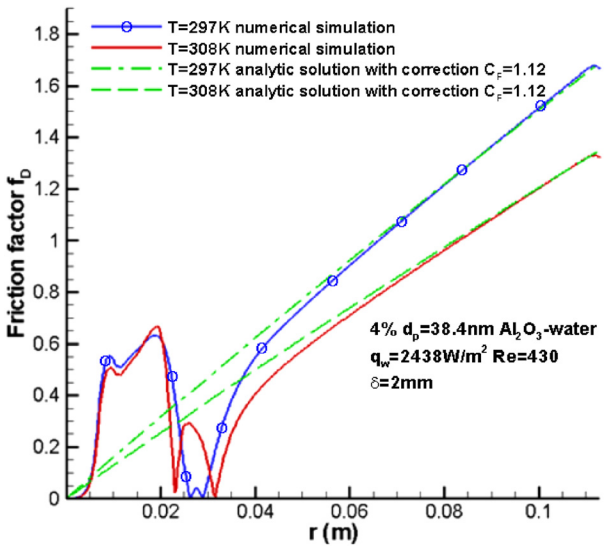

Fig. 8 Friction factor comparisons between correlated theoretical prediction and numerical simulations for nanofluids with different inlet temperatures

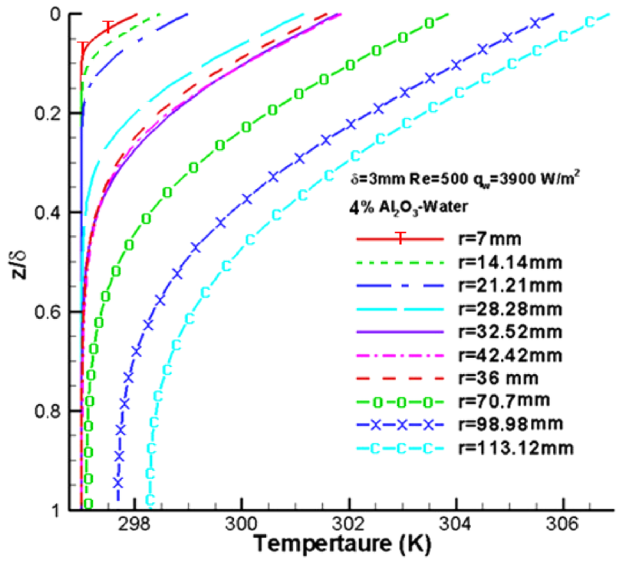

Fig. 9 Heat transfer and frictional entropy generation rate for Al_2O_3-water nanofluids with different nanoparticle volume fractions

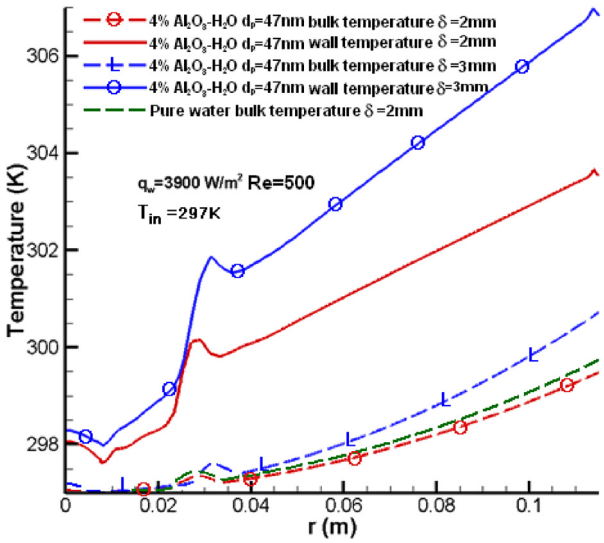

Fig. 10 Comparison of wall temperatures and bulk temperatures between two parallel disks along the r-direction for 4% Al_2O_3-water nanofluid with $\delta = 2$ mm and $\delta = 3$ mm

capture the effect of the complex flow field (Fig. 7) on f_D, while for $r > 0.06$ m analytic and numerical F_D solutions match for both disk gaps and inlet temperatures. With elevated T_{in} values the friction factor f_D in the r-direction is reduced. Clearly, the increase of T_{in} leads to the decrease of the dynamic viscosity which causes a decrease in wall shear stress (see Eq. (30)). Such a phenomenon indicates that dealing with nanofluids at relatively high temperatures can reduce wall shear stresses, which will also result in better heat transfer efficiencies. Furthermore, although differences can be observed between theoretical predictions for f_D (Eq. (33)) and the numerical simulation results in the quasi fully-developed flow region, the trends, due to the increase in inlet flow temperature, can be well predicted by Eq. (33).

With the increase in nanoparticle volume fraction φ the heat transfer performance of nanofluids improves, leading to a decrease in fluid bulk temperature. However, the viscosity and hence the friction factor increase, which may require a slightly higher pumping power. Clearly, compared the solution of Eq. (33), numerical simulation results of dilute nanofluid suspensions predict higher wall shear stress and f_D values. Nevertheless, a friction factor correlation for fully-developed Al_2O_3-water nanofluid flow between parallel disks can be proposed as

$$f_D = C_F \cdot \frac{96}{Re_{nf}^{in}} \cdot \frac{2\delta}{R_{in}} \cdot \frac{r}{R_{in}} \tag{46}$$

where $C_F = 1.12$ is the correction constant, and Eq. (46) holds for T_{in} from 297 K to 315 K, d_p from 30 nm to 47 nm, Re_{nf}^{in} from 300 to 500, and φ from 0.01 to 0.04 (see Fig. 8).

4.4 Temperature Fields

4.4.1 Temperature Profile Development Between Parallel Disks. The development of the gap-temperature profile in the r-direction is shown in Fig. 9. As expected, at the upper heated disk ($z = 0$), the slope of T is constant because the prescribed wall heat flux, while at the lower adiabatic disk ($z = 3$ mm) the slope is zero. Starting from $r = 0$, the uniform temperature region, i.e., the so-called unheated zone, shrinks as r increases. After the unheated zone has disappeared, the lower disk's temperature begins to increase from 297 K. However, between $r = 20$ mm and $r = 40$ mm, where the recirculation cell exists, the wall temperature suddenly increases and then is reduced without influencing the wall temperature of the lower disk; because, at this range, the lower disk is not influenced by the heat transferred from the upper disk.

4.4.2 Temperature Fields versus Disk-Spacing. The numerical solutions for the wall and bulk temperatures, considering the two disk gaps, are shown in Fig. 10. It can be observed that both temperatures for $\delta = 3$ mm are higher than those for $\delta = 2$ mm. The same trend was reported by Gherasim et al. [2] for the wall temperature. As δ decreases the average flow velocity $\bar{v}$ increases, leading to more rapid convective heat transfer in the r-direction. Hence, the $\delta = 2$ mm cooling system generates a better heat transfer performance than $\delta = 3$ mm. Also, when employing Al_2O_3-water nanofluids in $\delta = 2$ mm cooling channels a lower bulk temperature is achieved, indicating that the nanofluid provides improved convective heat transfer performance when compared to pure water.

Further computational analyses [14] showed that with smaller nanoparticle diameters and higher volume fractions the wall temperature decreases as well.

4.5 Nusselt Number. For nanofluids, the Nusselt number is defined as

$$Nu_{nf} = \frac{h_{nf} D_h}{k_{water}} \tag{47}$$

where the nanofluid heat transfer coefficient h_{nf} is given as

$$h_{nf} = \frac{q_w}{T_w - T_b} \tag{48}$$

Here, q_w is the wall heat flux, T_w is the wall temperature, and T_b is the nanofluid bulk temperature.

Considering again 4% Al_2O_3-water nanofluids with different particle diameters, i.e., $d_p = 30$ nm and 47 nm, Fig. 11 demonstrates that the use of nanofluids is advantageous over pure water. Specifically, the heat transfer coefficient (and hence the Nusselt number) increases with a decrease in nanoparticle diameter and with higher Reynolds numbers. As expected, the parallel disk entrance region with its complex flow field exhibits greatly nonlinear Nu(r) variations (see also Fig. 10).

4.6 Entropy Generation Analysis. As mentioned, minimization of entropy generation via operational and/or geometric changes is a modern system design tool. For the present jet-impingement, parallel disk device it is of interest to analyze the effects of the nanoparticle volume fraction and inlet Reynolds number on entropy generation due to both friction and heat transfer [16,18].

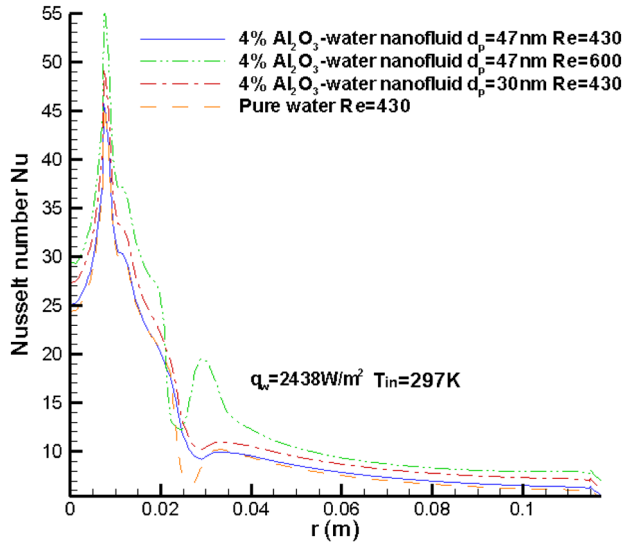

Fig. 11 Nusselt number Nu_{nf} comparison between Al_2O_3-water nanofluids with different inlet Reynolds numbers, particle diameters, and volume fraction

4.6.1 Entropy Generation versus Nanoparticle Volume Fraction. Pure water, as well as 2% and 4% $d_p = 38.4$ nm Al_2O_3-water nanofluids were investigated for the influence of nanoparticle volume fraction φ on the entropy generation rate in the cooling system (see Fig. 1(a)). Figure 12 shows the heat transfer and frictional entropy generation rates in the whole flow domain, where Entropy Generation (see Eq. (42)) decreases with the increase in volume fraction. It indicates that the use of nanofluids as coolants provides higher heat transfer efficiencies than pure water in light of the fact that entropy generation is equivalent to waste production.

4.6.2 Entropy Generation versus Nanofluid Inlet Reynolds Number. For the 4% $d_p = 47$ nm Al_2O_3-water case considering different inlet Reynolds numbers (i.e., $Re_{nf}^{in} = 150$, 200, 300, 430, 500, 600, 700, and 800), it is shown that entropy generation rate due to heat transfer $\dot{S}_{gen}^{'''(H)}$ nonlinearly decreases while $\dot{S}_{gen}^{'''(F)}$ nonlinearly increases (Fig. 13). The reason is that with the increase of inlet Reynolds number, the nanofluid provides an improved heat transfer performance which leads to a lower temperature gradient between parallel disks, whereas the velocity gradient $\partial v_r/\partial r$ increases. Thus, according to Eqs. (43*a*) and (43*b*), the decrease

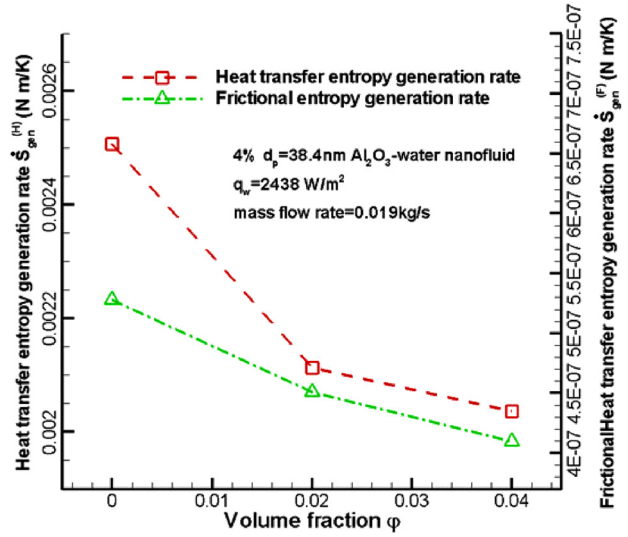

Fig. 12 Temperature profiles development between two parallel disks along the r-direction for 4% Al_2O_3-water nanofluid

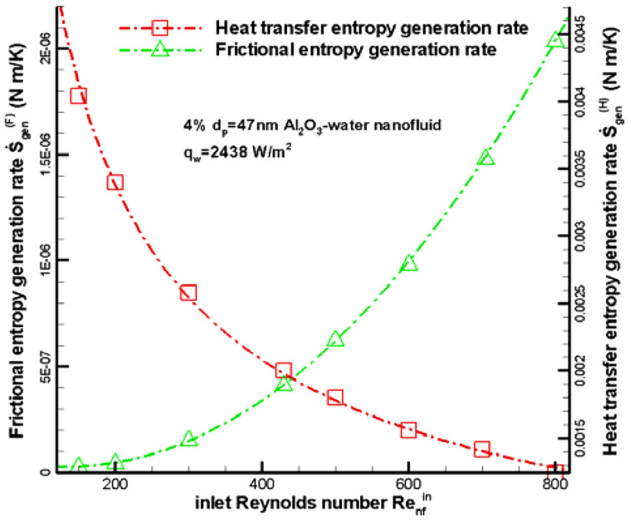

Fig. 13 Heat transfer and frictional entropy generation rate for 4% $d_p = 47$ nm Al_2O_3-water nanofluids with different inlet Reynolds numbers

of temperature gradients causes the decrease of $\dot{S}_{gen}^{(H)}$ and the increase in velocity gradients causes the increase in $\dot{S}_{gen}^{(F)}$. Due to the demonstrated fact that $\dot{S}_{gen}^{'''(F)} \ll \dot{S}_{gen}^{(H)}$, the total entropy generation rate decreases with the increase of inlet Reynolds number.

Additionally, the influence of inlet temperature on the entropy generation rate was investigated by comparing the numerical results for $T_{in} = 297$ K and $T_{in} = 308$ K [14]. An increase in nanofluid inlet temperature reduces the total entropy generation rate, both $\dot{S}_{gen}^{'''(F)}$ and $\dot{S}_{gen}^{'''(H)}$.

5 Conclusions

Using the new, experimentally validated F-K model (Part I) for the enhanced thermal conductivity of nanofluids, k_{nf}, numerical simulations have been performed investigating the convective heat transfer performance of Al_2O_3-water nanofluid flow between parallel disks. With the increment of inlet Reynolds number, the complex flow field near the center of the parallel disks essentially influences the heat transfer performance of the coolant. A new correction factor has been provided to predict the friction factor of nanofluids. The convective heat transfer performance improves with higher nanoparticle volume fraction, smaller nanoparticle diameter, and elevated bulk temperature. In addition, an entropy generation analysis is presented which shows that nanofluids are able to enhance the efficiency of the present cooling device over the use of conventional base fluids. Considering also the negligible increment in pressure drop when using nanofluids, they are promising new coolants which can generate better convective heat transfer performances and hence cooling efficiencies.

Acknowledgment

The authors appreciate and acknowledge the use of ANSYS (V. 11 and V. 12) from ANSYS Inc. (Canonsburg, PA), made available by Dr. Helen Redshaw (Department of Domestic Partnerships). Also, the authors appreciate and acknowledge the Chinese Scholarship Council (CSC) for financial support of Yu Feng.

References

[1] Kleinstreuer, C., and Li, J., 2008, "Microscale Cooling Devices," *Encyclopedia of Microfluidics and Nanofluidics*, D. Li, ed., Springer-Verlag, Heidelberg, Germany.
[2] Gherasim, I., Roy, G., Nguyen, C. T., and Vo-Ngoc, D., 2009, "Experimental Investigation of Nanofluids in Confined Laminar Radial Flows," Int. J. Therm. Sci., **48**, pp. 1486–1493.
[3] Winter, H. H., 1975, "Approximate Calculation and Measurement of the Pressure Distribution in Radial Flow of Molten Polymers Between Parallel Discs," Polym. Eng. Sci., **15**(6), pp. 460–469.

[4] Szeri, A. Z., Schneider, S. J., Labbe, F., and Kaufman, H. N., 1983, "Flow Between Rotating Disks, Part 1: Basic Flow," J. Fluid Mech., **134**, pp. 103–131.
[5] Mochizuki, S., and Yang, W. J., 1987, "Local Heat-Transfer Performance and Mechanisms in Radial Flow Between Parallel Disks," J. Thermophys., **1**(2), pp. 112–115.
[6] Nakabayashi, K., Ichikawa, T., and Morinishi, Y., 2002, "Size of Annular Separation Bubble Around the Inlet Corner and Viscous Flow Structure Between Two Parallel Disks," Exp. Fluids, **32**, pp. 425–433.
[7] Achintya, M., 2009, "Analytical Solutions of Nusselt Number for Thermally Developing Radial Flow Through Small Gap Between Two Parallel Disks," J. Heat Transfer, **131**, p. 054502.
[8] Roy, G., Nguyen, C. T., and Lajoie, P.-R., 2004, "Numerical Investigation of Laminar Flow and Heat Transfer in a Radial Flow Cooling System With the Use of Nanofluids," Superlattices Microstruct., **35**, pp. 497–511.
[9] Roy, G., Palm, S. J., and Nguyen, C. T., 2005, "Heat Transfer and Fluid Flow of Nanofluids in Laminar Radial Flow Cooling Systems," J. Therm. Sci., **14**(4), pp. 362–367.
[10] Maiga, S. E. B., Palm, S. J., Nguyen, C. T., Roy, G., and Galanis, N., 2005, "Heat Transfer Enhancement by Using Nanofluids in Forced Convection Flows," Int. J. Heat Fluid Flow, **26**, pp. 530–546.
[11] Palm, S. J., Roy, G., and Nguyen, C. T., 2006, "Heat Transfer Enhancement With the Use of Nanofluids in Radial Flow Cooling Systems Considering Temperature-Dependent Properties," Appl. Therm. Eng., **26**, pp. 2209–2218.
[12] Li, J., 2008, "Computational Analysis of Nanofluid Flow in Microchannels With Applications to Micro-Heat Sinks and Bio-MEMS," Ph.D. thesis, North Carolina State University, Raleigh, NC.
[13] Maxwell, J. C., 1891, *A Treatise on Electricity and Magnetism*, 3rd ed., Clarendon Press, Oxford, UK.
[14] Feng, Y., 2009, "A New Thermal Conductivity Model for Nanofluids With Convection Heat Transfer Application," M.S. thesis, NC State University, Raleigh, NC.
[15] Turns, S. R., 2006, "Entropy Generation Analysis for Nanofluid Flow in Microchannels," ASME, J. Heat Transfer (in press).
[16] Li, J., and Kleinstreuer, C., 2010, "Entropy Generation Analysis for Nanofluid Flow in Microchannels," ASME J. Heat Transfer, **132**(12), pp. 122401-1–8.
[17] McGinn, J. H., 1956, "Observations on the Radial Flow of Water Between Fixed Parallel Plates," Appl. Sci. Res., Sect. A, **5**, pp. 255–264. Available at: http://www.springerlink.com/content/84522n24314r20n3/
[18] Bejan, A., 1996, *Entropy Generation Minimization*, CRC Press, Inc., Boca Raton, FL.